MDPI

Article

Mechanical Behavior and Thermal Stability of (AlCrTiZrMo)N/ZrO$_2$ Nano-Multilayered High-Entropy Alloy Film Prepared by Magnetron Sputtering

Qingqing Zhai [1], Wei Li [1],*, Ping Liu [1], Wenjie Cheng [1], Ke Zhang [1], Fengcang Ma [1], Xiaohong Chen [1], Rui Feng [2] and Peter K. Liaw [3]

[1] School of Materials Science and Engineering, University of Shanghai for Science and Technology, Shanghai 200093, China; zqq780823@163.com (Q.Z.); liuping@usst.edu.cn (P.L.); cwj201850156@gmail.com (W.C.); zhangke@usst.edu.cn (K.Z.); mafengcang@163.com (F.M.); cxh992@163.com (X.C.)
[2] Oak Ridge National Laboratory, Neutron Scattering Division, Oak Ridge, TN 37831, USA; fengruisjtu@gmail.com
[3] Department of Materials Science and Engineering, The University of Tennessee, Knoxville, TN 37996, USA; pliaw@utk.edu
* Correspondence: liwei176@usst.edu.cn; Tel.: +86-21-55271682

Abstract: A new type of high-entropy alloy, a nitride-based (AlCrTiZrMo)N/ZrO$_2$ nano-multilayered film, was designed to investigate the effect of ZrO$_2$ layer thickness on the microstructure, mechanical properties, and thermal stability. The results show that when the thickness of the ZrO$_2$ layer is less than 0.6 nm, it can be transformed into cubic-phase growth under the template effect of the (AlCrTiZrMo)N layer, resulting in an increased hardness. The (AlCrTiZrMo)N/ZrO$_2$ film with a ZrO$_2$ layer thickness of 0.6 nm has the highest hardness and elastic modulus of 35.1 GPa and 376.4 GPa, respectively. As the thickness of the ZrO$_2$ layer further increases, ZrO$_2$ cannot maintain the cubic structure, and the epitaxial growth interface is destroyed, resulting in a decrease in hardness. High-temperature annealing treatments indicate that the mechanical properties of the film decrease slightly after annealing at less than 900 °C for 30 min, while the mechanical properties decrease significantly after annealing for 30 min at 1000–1100 °C. The hardness and elastic modulus after annealing at 900 °C are still 24.5 GPa and 262.3 GPa, showing excellent thermal stability. This conclusion verifies the "template" effect of the nano-multilayered film, which improves the hardness and thermal stability of the high-entropy alloy.

Keywords: (AlCrTiZrMo)N/ZrO$_2$; nano-multilayered film; microstructure; mechanical properties; thermal stability

1. Introduction

In 2004, Yeh et al. [1] and Cantor et al. [2] proposed a multi-component high-entropy alloy (HEA). The new class of alloys generally consists of 5–13 elements, and the atomic-composition ratio of each component is between 5% and 35%, which exhibits a simple face-centered cubic (fcc), body-centered cubic (bcc), or hexagonal close-packed (hcp) crystalline phase rather than an intermetallic compound after solidification [2–8]. Many studies have shown that, compared to conventional alloys, HEAs have better strength [9], hardness [10], wear [11–13], fatigue [14–17], and corrosion resistance [18–21]; good plasticity [22,23] and fracture toughness [24–26]; and high electrical resistivity [27,28]. The field of high-entropy alloys has inspired scholars to explore multi-element alloys. Different constituent elements will show different microstructural characteristics and mechanical properties, and the superior performance of HEAs has attracted more and more attention [29].

Due to the exhibited outstanding properties of HEAs, HEA films have also received increasing attention in the application of protective coatings [30]. The attractive performance

of HEA nitride films has especially been highly valued. Schwarz et al. [31] studied the composition of a CoCrFeNi high-entropy alloy using different methods, and they found that the stoichiometry, phase composition, and microscopic structure of the as-deposited HEA thin films are almost identical if the same deposition parameters are used. Chen et al. [32] used FeCoNiCrCuAlMn and FeCoNiCrCuAl as sputtering targets to deposit a nitride film. The alloy film was crystalline and appeared as fcc or a mixed phase of fcc and bcc. As the nitrogen flow rate increases, the crystallinity of the nitride film decreases and approaches an amorphous state. Huang et al. [33] prepared an AlCrNbSiTiV alloy and its nitride film by reactive radio frequency unbalanced magnetron sputtering, which presented amorphous and fcc structures. The maximum hardness and elastic modulus of the nitride film reached 41 GPa and 360 GPa, respectively. Liang et al. [34] fabricated different (TiVCrZrHf)N coatings by reactive magnetron sputtering. At low nitrogen flow rates, the film exhibited an amorphous structure, and when the flow rate increased to 4 sccm (standard-state cubic centimeter per minute) or higher, the films presented a columnar structure of the fcc phase, and the hardness and elastic modulus reached the maximum values of 23.8 GPa and 267.3 GPa, respectively. The constituent elements of the HEA are divided into nitride-forming elements and non-nitride-forming elements. The nitride-forming elements tend to react with nitrogen to form ceramic phases, resulting in an improvement in the mechanical properties of the film.

With the rapid development of technology in the industry, the working environment of tools has become harsher, and the protective coating needs to have more comprehensive properties, such as hardness, wear resistance, thermal stability, and corrosion resistance. Traditional monolayered binary or ternary coatings are difficult to meet the requirements when they are required to work in harsh working conditions. Koehler [35] proposed the concept of a nano-multilayered film in 1970. Nano-multilayered films are formed by alternately depositing two materials with nanoscale thickness. The thickness of two different layers is called the modulation period. In 1977, Yang et al. [36] fabricated Au-Ni and Cu-Pd nano-multilayered films, and their hardness and elastic modulus both unusually improved. Chu et al. [37] prepared a TiN/Ni nano-multilayered film and found that the hardness of the film increased to 3500 kgf mm^{-2} when the modulation period was 2.2 nm.

Sputtering is a non-thermal evaporation process that ejects atoms from the target surface by the momentum transfer of atomic-sized high-energy bombarding particles (usually gaseous ions accelerated by plasma). Therefore, substrate does not deform because of the excessive deposition temperature. Direct current (DC) magnetron sputtering is mainly used to sputter metal materials; however, radio frequency (RF) magnetron sputtering, which confines the motion of secondary electrons to near the target surface by a magnetic field, can sputter almost all materials, including semiconductors, insulators, and conductors [38]. Zirconia (ZrO$_2$) is a type of ceramic material that has three structures, namely, monoclinic, tetragonal, and cubic phases, and it has high hardness, elevated temperature resistance [39], and low thermal conductivity [40]. It can be used as a high-temperature insulation material. Therefore, the addition of a ZrO$_2$ layer into a nano-multilayered film is expected to improve the thermal stability and mechanical properties by magnetron sputtering. The constituent elements of an AlCrTiZrMo alloy are all composed of nitride-forming elements, and they can form a ceramic phase with a higher hardness with nitrogen atoms. Therefore, in this study, (AlCrTiZrMo)N is selected as the template layer of the nano-multilayered film, and ZrO$_2$ is used as the modulation layer. (AlCrTiZrMo)N/ZrO$_2$ nano-multilayered films with different ZrO$_2$ layer thicknesses are prepared, which is expected to improve the mechanical properties and high-temperature resistance of the (AlCrTiZrMo)N/ZrO$_2$ nano-multilayered film.

2. Materials and Methods

The equiatomic AlCrTiZrMo HEA target was prepared by vacuum arc melting under a pure Ar atmosphere, with each component having a purity of at least 99.99% (weight percent). The ZrO$_2$ target was prepared by powder metallurgy with a purity of at least

99.99% (weight percent). The (AlCrTiZrMo)N layers were deposited from an AlCrTiZrMo HEA target by DC mode, and the power was set at 100 W. The ZrO_2 layers were sputtered from the ZrO_2 target by RF mode, and the power was set at 150 W. The film was deposited on a single-crystal silicon wafer with the size of 30 mm $\times$ 20 mm $\times$ 1 mm. The silicon wafer was cleaned before the deposition. Primarily, the silicon wafer was immersed in ethanol and then placed in an ultrasonic cleaning chamber for 15 min. After drying, the silicon wafer was placed in a vacuum chamber for reverse sputtering cleaning. The N_2 and Ar flow rates were 15 sccm and 20 sccm, respectively, with a working pressure of 0.6 Pa. The sputtering rate of ZrO_2 under the experimental condition was 0.1 nm/s based on a cross-sectional TEM observation. By controlling the deposition time of the ZrO_2 layer, (AlCrTiZrMo)N/ZrO_2 nano-multilayered films with ZrO_2 thicknesses of 0.2 nm, 0.4 nm, 0.5 nm, 0.6 nm, 0.7 nm, 0.8 nm, 1 nm, and 1.2 nm were obtained. The film thickness was about 2 μm. Under the same condition, a monolithic (AlCrTiZrMo)N film with a thickness of about 2 μm was prepared for comparison. Figure 1 is a schematic illustration of the (AlCrTiZrMo)N/ZrO_2 nano-multilayered film, in which Λ is the modulation period.
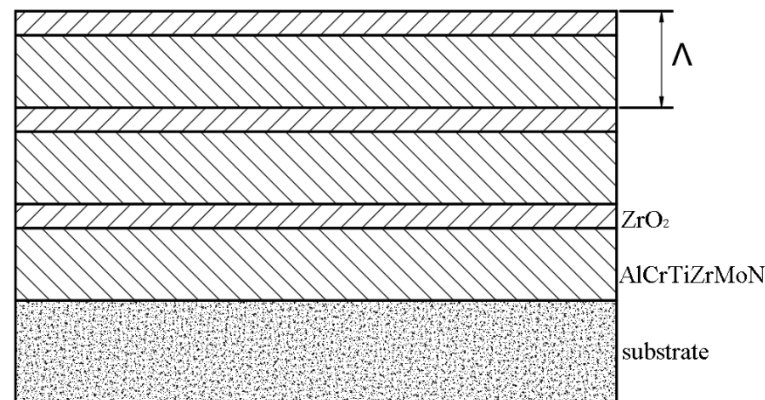

Figure 1. Schematic illustration of the (AlCrTiZrMo)N/ZrO_2 nano-multilayered film.

The microstructures of (AlCrTiZrMo)N/ZrO_2 nano-multilayered films and monolithic (AlCrTiZrMo)N films were characterized by the D8 Advance X-ray diffractometer (XRD, Bruker, Mannheim, Germany) using CuK_α radiation (λ = 0.15406 nm), the Quanta FEG450 field-emission environmental electron microscope (SEM, FEI, Hillsboro, OR, USA), and Tecnai G220 high-resolution field-emission transmission electron microscope (HRTEM, FEI, Hillsboro, OR, USA). The XRD patterns were measured using the Bragg–Brentano (θ/2θ) scan mode with parameters of 30 kV and 20 mA. The diffraction angle of the XRD pattern ranges from 25° to 90°. The elemental distributions were analyzed by an electron probe microanalyzer (EPMA, JXA-8530F PLUS, Tokyo, Japan). The hardness and elastic modulus of the films were measured by a G200 nano-indentation system (Agilent, Santa Clara, CA, USA). A Berkovich diamond indenter was used with a loading rate of 0.05/s, a load of 5 mN, and a press-in depth of 100 nm, which was less than 1/10 of the film thickness so that the influence of the substrate on the mechanical properties of the film could be eliminated. At least 16 points were selected for the hardness measurement of each film, and the data with a coefficient of variation of less than 10% were selected to calculate the average hardness value of the film. In order to evaluate the thermal stability of the (AlCrTiZrMo)N/ZrO_2 nano-multilayered film, the sample was placed in a furnace and annealed in air for 30 min at 700 °C, 800 °C, 900 °C, 1000 °C, and 1100 °C. The sample was then removed, placed in air, and cooled to room temperature at a cooling rate of about 100 °C/min. The structural changes and mechanical properties of the annealed samples were measured by the XRD and nanoindentation techniques. Table 1 shows the deposition parameters and the element contents of the (AlCrTiZrMo)N/ZrO_2 nano-multilayered films.

Table 1. The deposition parameters and the element contents of the (AlCrTiZrMo)N/ZrO$_2$ nano-multilayered films.

Sample	N$_2$/Ar (sccm)	P (Pa)	DC/RF (W)	Modulation (nm)	Film (μm)	Al At%	N At%	Zr At%	Ti At%	Mo At%	Cr At%	O At%
AlCrTiZrMoN	15/20	0.6	100		2	7.95	13.11	5.21	6.37	6.41	6.60	54.35
(AlCrTiZrMo)N/ZrO$_2$	15/20	0.6	100/150	0.2	2	6.02	8.75	5.17	4.62	5.57	5.30	64.58
(AlCrTiZrMo)N/ZrO$_2$	15/20	0.6	100/150	0.4	2	6.54	11.73	5.73	5.67	5.83	5.65	58.87
(AlCrTiZrMo)N/ZrO$_2$	15/20	0.6	100/150	0.6	2	6.75	12.29	5.99	5.88	5.88	5.73	57.48
(AlCrTiZrMo)N/ZrO$_2$	15/20	0.6	100/150	0.8	2	6.85	11.21	6.22	5.78	5.93	5.90	58.12
(AlCrTiZrMo)N/ZrO$_2$	15/20	0.6	100/150	1.2	2	6.84	12.63	6.78	5.69	6.01	5.83	56.22

3. Results

3.1. Microstructures

In Figure 2, the values of the ZrO$_2$ thicknesses are marked on their corresponding XRD patterns. The monolithic (AlCrTiZrMo)N film and the (AlCrTiZrMo)N/ZrO$_2$ nano-multilayered films present an fcc structure. The diffraction peaks of the monolithic (AlCrTiZrMo)N film are weak. As the thickness of the ZrO$_2$ layer increases, the (111) and (200) peaks of the (AlCrTiZrMo)N/ZrO$_2$ nano-multilayered films first become large and then small. When the ZrO$_2$ layer thickness is 0.6 nm, the peak intensity reaches the maximum value. According to the previous reports of nano-multilayered films [41], it can be inferred that when the ZrO$_2$ layer thickness is less than 0.6 nm, the ZrO$_2$ layer changes from a monoclinic structure to an fcc metastable structure under the template effect of the (AlCrTiZrMo)N layer, and it forms co-epitaxial growth with the (AlCrTiZrMo)N layers. Therefore, the crystallinity is improved, and, correspondingly, the intensity of the diffraction peak becomes strong. However, when the ZrO$_2$ layer thickness is more than 0.6 nm, the effect of the improved crystallinity of the nano-multilayered film gradually disappears. Therefore, the crystallinity becomes generally weak, and the intensity of the diffraction peak tends to decrease. It can also be seen in Figure 2 that the (AlCrTiZrMo)N/ZrO$_2$ nano-multilayered film shows a shift toward a lower angle in the (111) diffraction peak when the ZrO$_2$ layer thickness is 0.6 nm.
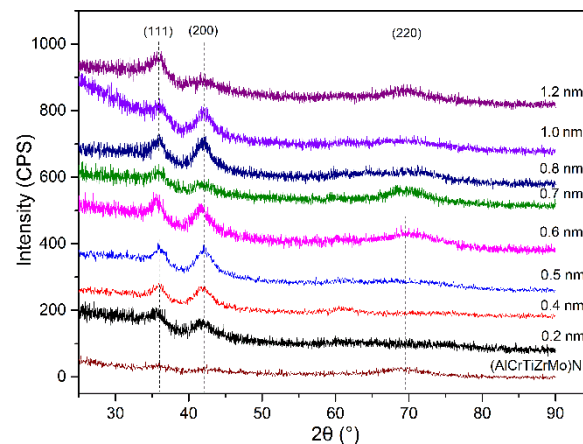
Figure 2. XRD patterns of the (AlCrTiZrMo)N/ZrO$_2$ nano-multilayered films with different ZrO$_2$ layer thicknesses.

The crystal structure transition of ZrO$_2$ occurs due to the "template effect" of the nano-multilayered film. The (AlCrTiZrMo)N layer has a stable fcc crystal structure. Since the thickness of the modulation layer generally does not exceed a few nanometers, the nucleation and growth of the ZrO$_2$ layer are greatly affected by the structure of the template layer. When the ZrO$_2$ layer is nucleated, the total energy per unit area of the ZrO$_2$ layer, E_T, can be expressed as [42]

$$E_T = E_B t + E_I \tag{1}$$

where E_B is the volume free energy of ZrO_2, t is the thickness of the ZrO_2 layer, and E_I is the interfacial energy. When ZrO_2 starts to deposit, $t \rightarrow 0$, E_I is the main part of E_T. Compared with the ZrO_2 of the monoclinic structure, the interface energy of the cubic-structured ZrO_2 and (AlCrTiZrMo)N is smaller. Therefore, ZrO_2 tends to grow epitaxially in the cubic structure. As a result, the crystal growth of the (AlCrTiZrMo)N layer is promoted, and the intensity of the cubic-phase diffraction peak is enhanced as can be seen in Figure 2. However, as the thickness of the ZrO_2 layer increases, E_B becomes larger, and E_I is no longer the main part of E_T. ZrO_2 nucleates and grows on the surface of the (AlCrTiZrMo)N layer, and the effect of the volume free energy becomes increasingly evident. When the critical thickness reaches 0.6 nm, the total energy of the cubic structure of ZrO_2 is greater than that of the monoclinic structure of ZrO_2. As a result, ZrO_2 is converted to monoclinic phase growth, and the crystallinity of the (AlCrTiZrMo)N layer is lowered, and the intensity of the cubic-phase diffraction peak is weakened when the thickness of ZrO_2 is more than 0.6 nm. It should be noted that Figure 2 does not detect the diffraction peak of the monoclinic phase of ZrO_2, probably because the thickness of ZrO_2 is too small to be detected.

　　Figure 3 presents the HRTEM images of the cross-sectional morphology of the (AlCrTiZrMo)N/ZrO_2 nano-multilayered film with the ZrO_2 layer thickness of 0.6 nm. In the low-magnified image of Figure 3a, the (AlCrTiZrMo)N/ZrO_2 nano-multilayered film has a good columnar structure along the direction of the film growth. The width of the columnar crystal is about 20–50 nm, the length runs through several modulation periods of the nano-multilayered film, and the insertion of the ZrO_2 layer does not damage the columnar crystal growth. Figure 3b presents the medium-magnified cross-sectional morphology, which indicates a well-grown nano-multilayered film structure. The layers with the gray contrast are (AlCrTiZrMo)N, and the ones with the bright contrast refer to ZrO_2. The (AlCrTiZrMo)N and the ZrO_2 layers are alternately deposited to form a continuous nano-multilayered film structure. Figure 3c presents a high-magnified HRTEM image from the selected area of Figure 3b. The modulation period of the nano-multilayered film is measured as 8 nm, and the nanocrystal distribution is very dense and uniform. Chu et al. [43] calculated the hardness behavior of multilayered film, and the hardness was significantly improved when Λ = 5~10 nm. The lattice fringes can continuously move across several modulation periods, indicating that the ZrO_2 layer transforms into an fcc structure under the "template effect" of the (AlCrTiZrMo)N layers and grows epitaxially with them. The (111), (200), and (220) fcc-structured diffraction rings are presented in the selected area electron diffraction (SAED) patterns of Figure 3d, which are consistent with the results in the XRD patterns.
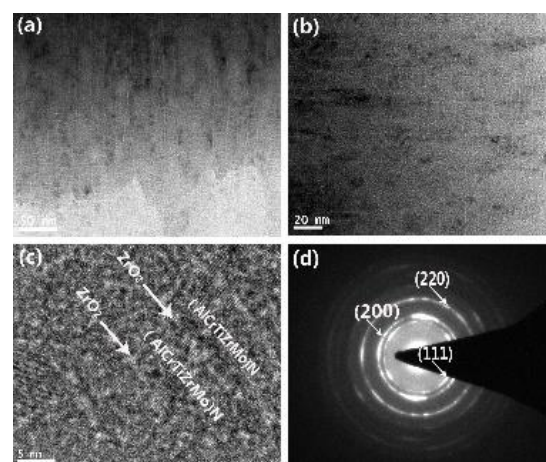

Figure 3. Cross-sectional HRTEM images of the (AlCrTiZrMo)N/ZrO_2 nano-multilayered film with the ZrO_2 layer thickness of 0.6 nm: (**a**) low magnification, (**b**) medium magnification, (**c**) high magnification, and (**d**) selected electron diffraction pattern.

The cross-sectional SEM morphology of the nano-multilayered films with various ZrO_2 layer thicknesses is presented in Figure 4. In Figure 4a, when the ZrO_2 layer thickness is 0.2 nm, the columnar crystals cannot be clearly observed in the cross-sectional image. The thickness of the ZrO_2 layer in Figure 4b is 0.4 nm, which shows a clear columnar crystal structure. As the ZrO_2 layer thickness increases, the ZrO_2 layer gradually transforms into an fcc structure under the "template effect" of the (AlCrTiZrMo)N layer. Therefore, the crystallinity is improved. When the thickness of the ZrO_2 layer of the nano-multilayered film in Figure 4c is 0.6 nm, the columnar crystal growth of the nano-multilayered film is complete, suggesting that the insertion of the ZrO_2 layer does not destroy the columnar growth feature of the (AlCrTiZrMo)N film, which is consistent with the XRD patterns. However, as the thickness of the ZrO_2 layer continues to increase, the columnar crystal structure in Figure 4d,e begins to weaken, indicating that the crystallinity deteriorates, which is in accordance with the XRD results.
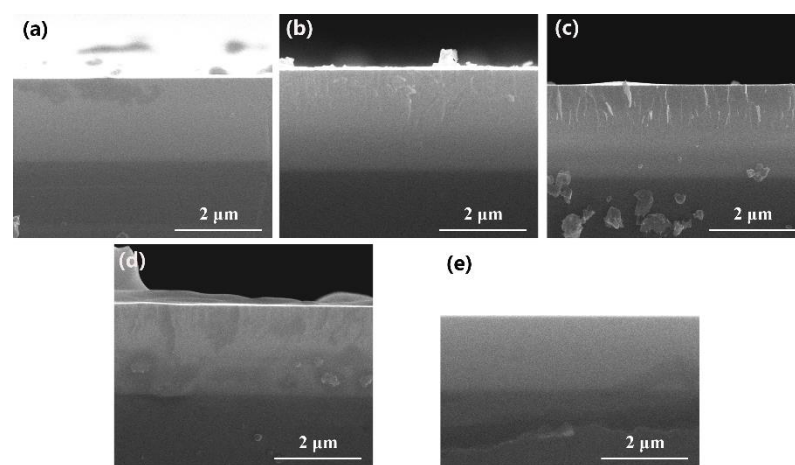

Figure 4. Cross-sectional SEM images of nano-multilayered films with different ZrO_2 thicknesses: (**a**) 0.2 nm, (**b**) 0.4 nm, (**c**) 0.6 nm, (**d**) 0.8 nm, and (**e**) 1.2 nm.

3.2. Mechanical Properties

Figure 5 shows the hardness and elastic modulus of the (AlCrTiZrMo)N/ZrO_2 nano-multilayered films with the different ZrO_2 layer thicknesses. The hardness and elastic modulus of the (AlCrTiZrMo)N film are 27.5 GPa and 260.2 GPa, respectively. When the thickness of the ZrO_2 layer is 0.2 nm, the hardness and elastic modulus of the nano-multilayered film are slightly lower than those of the monolithic (AlCrTiZrMo)N film, which is due to the fact that the integrity of the crystal growth of the (AlCrTiZrMo)N film is destroyed, which is a result of the insertion of thin ZrO_2 layers. With an increase in ZrO_2 layer thickness, the hardness and elastic modulus of the nano-multilayered film gradually increase, and they reach the maximum levels of 35.1 GPa and 376.4 GPa, respectively, when the ZrO_2 layer thickness is 0.6 nm. The strengthening effect can be attributed to the fact that the ZrO_2 layers transform into an fcc metastable structure under the "template effect" of the (AlCrTiZrMo)N layers, and they form co-epitaxial growth with the (AlCrTiZrMo)N layers, which promotes the film's integrity and blocks the dislocation movements. When the ZrO_2 layer thickness exceeds 0.6 nm, the ZrO_2 layers transform back into a stable monoclinic phase structure, and the co-epitaxial growth of the nano-multilayered film can no longer be maintained, leading to the disappearance of the strengthening effect. Accordingly, the hardness and elastic modulus of the nano-multilayered film decrease.
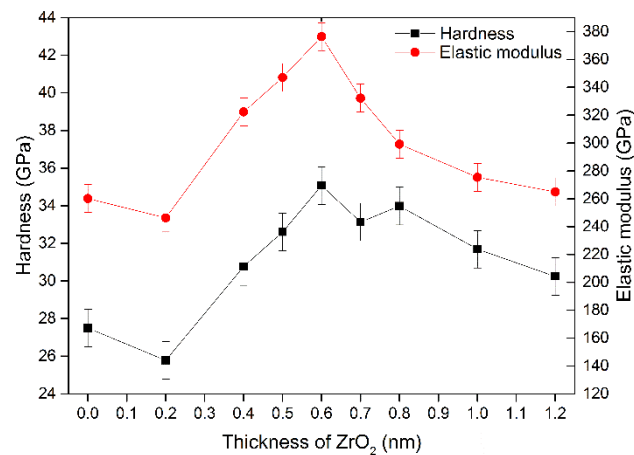
Figure 5. Variation of the hardness and elastic modulus of the (AlCrTiZrMo)N/ZrO$_2$ nano-multilayered films along with the ZrO$_2$ layer thickness.

3.3. Thermal Stability

To evaluate the thermal stability of the (AlCrTiZrMo)N/ZrO$_2$ nano-multilayered film, the (AlCrTiZrMo)N/ZrO$_2$ nano-multilayered film with the ZrO$_2$ layer thickness of 0.6 nm was annealed in air at 700 °C, 800 °C, 900 °C, 1000 °C, and 1100 °C for 30 min. The XRD patterns of the annealed films can be seen in Figure 6. It can be observed that as the temperature increases, the number of XRD peaks of the oxides of the (AlCrTiZrMo)N/ZrO$_2$ nano-multilayered film increases, suggesting that the degree of oxidation rises with an increase in the annealed temperature. After annealing in the temperature range from 700 °C to 900 °C, based on the XRD patterns, only the ZrO$_2$ can be found in the annealed film, indicating that the nano-multilayered film is slightly oxidized, and the basic composition of the nano-multilayered film is not changed. After annealing at 1000 °C and 1100 °C, more oxides, such as SiO$_2$ and Al$_2$O$_3$, are found in the XRD patterns, indicating that the oxidation degree of the nano-multilayered film remarkably increases.
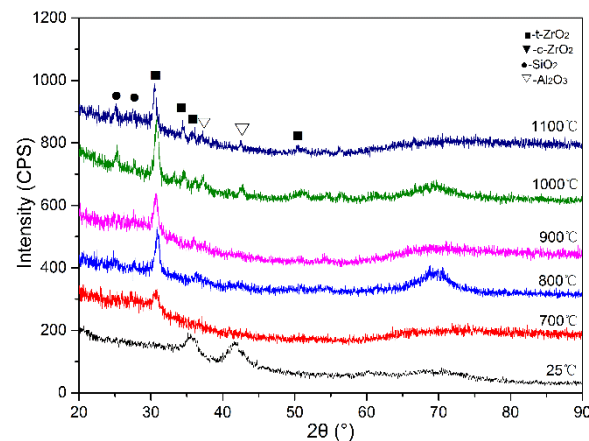

Figure 6. XRD patterns of the (AlCrTiZrMo)N/ZrO$_2$ nano-multilayered film with the ZrO$_2$ layer thickness of 0.6 nm after annealing at different temperatures for 30 min.

The hardness and elastic modulus of the (AlCrTiZrMo)N/ZrO$_2$ nano-multilayered film with the ZrO$_2$ layer thickness of 0.6 nm after annealing at different temperatures for 30 min are shown in Figure 7. In the annealing temperature range of 700–900 °C, the mechanical properties of the film decrease slightly. The hardness and elastic modulus of the (AlCrTiZrMo)N/ZrO$_2$ film at 900 °C are 24.5 GPa and 262.3 GPa, respectively. The indistinctive drop in mechanical properties can be attributed to the fact that the nano-multilayered film is only slightly oxidized. The hardness and elastic modulus of the

(AlCrTiZrMo)N/ZrO$_2$ film decrease rapidly following annealing at 1000–1100 °C. The hardness and elastic modulus of the films annealed at 1100 °C decrease to 9.8 GPa and 158.6 GPa, respectively. After annealing at 1000 °C or 1100 °C, more oxides are produced during the annealing process, suggesting that the (AlCrTiZrMo)N/ZrO$_2$ film is severely oxidized. As a result, the mechanical properties of the film degrade rapidly. It is worth noting that the mechanical properties of the (AlCrTiZrMo)N/ZrO$_2$ film after annealing at 900 °C are nearly equivalent to those of the monolithic (AlCrTiZrMo)N film at room temperature, indicating that the (AlCrTiZrMo)N/ZrO$_2$ film is stable at high temperatures and has a good high-temperature resistance.
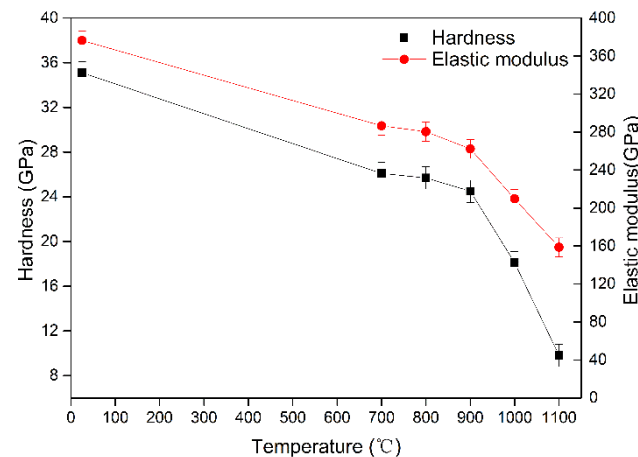

Figure 7. Variation of hardness and elastic modulus of the (AlCrTiZrMo)N/ZrO$_2$ nano-multilayered film with the ZrO$_2$ layer thickness of 0.6 nm after annealing at different temperatures for 30 min.

4. Discussion

4.1. Effect of Structures on Mechanical Properties of the (AlCrTiZrMo)N/ZrO$_2$ Nano-Multilayered Film

The modulus-difference strengthening theory [35] and the alternating stress field theory [44] can explain the strengthening phenomenon of the (AlCrTiZrMo)N/ZrO$_2$ nano-multilayered films.

Koehler [35] proposed the modulus-difference strengthening theory and suggested that when dislocations move across the coherent interface within the nano-multilayered film, they become subjected to the mirror force of the coherent interface. This force could be caused by the fact that the dislocations have different line energies in the layers with different shear moduli. Additional stress is required when the dislocations cross from the layer with a low shear modulus to that with a high shear modulus. Therefore, the dislocation movements can be hindered, and the nano-multilayered film becomes strengthened. The greater the difference in the shear modulus between the two layers, the more remarkable the strengthening effect. The shear modulus, *G*, can be expressed as

$$G = \frac{E}{2(1+v)} \tag{2}$$

where *E* is the elastic modulus, and *v* is the Poisson ratio. In this study, $E_{(AlCrTiZrMo)N}$ = 260.2 GPa, E_{ZrO2} = 160 GPa, and the Poisson ratio is 0.25; the shear moduli of (AlCrTiZrMo)N and ZrO$_2$ can be calculated as $G_{(AlCrTiZrMo)N}$ = 104.1 GPa and G_{ZrO2} = 64 GPa, respectively. According to the modulus-difference strengthening theory [45], the hardness increment (ΔH_1) relative to the layer with the lowest hardness can be calculated. In the (AlCrTiZrMo)N/ZrO$_2$ nano-multilayered film, the layer with the lowest hardness refers

to ZrO$_2$, and its hardness is measured as 11.5 GPa. The hardness increment (ΔH_1) can be expressed as [45]

$$\frac{(1-\nu)(G_A - G_B)\sin\theta}{m\pi^2} \leq \Delta H_1 \leq \frac{3(G_A - G_B)\sin\theta}{m\pi^2} \qquad (3)$$

For the (AlCrTiZrMo)N/ZrO$_2$ nano-multilayered films, $G_{(AlCrTiZrMo)N} > G_{ZrO2}$; thus, G_A is $G_{(AlCrTiZrMo)N}$, and G_B is G_{ZrO2}; θ is the angle between the slip surface of the low modulus layer and the coherent interface, taking 45° [45] in the investigation; m is the Taylor factor, and the nitride ceramic phase can take 0.3 [46]. According to the calculation, the hardness increment (ΔH_1) of the (AlCrTiZrMo)N/ZrO$_2$ nano-multilayered films, relative to ZrO$_2$, is 21.5–28.7 GPa.

Kato [44] introduced the theory of the alternating stress field to nano-multilayered films to explain the phenomenon of the hardness improvement. It is suggested that the stress field at the coherent interface of a nano-multilayered film could lead to the strengthening effect. Since (AlCrTiZrMo)N and ZrO$_2$ have different lattice constants, in order to achieve coherent growth at the interface, lattice mismatch occurs between the two layers of the materials, and the stress magnitude at the interface depends on the mismatch between the two layers. In a nano-multilayered film with a coherent structure, the layer with a larger lattice constant tends to become smaller and, thus, is subjected to compressive stress, while the layer with a smaller lattice constant is subjected to tensile stress. As shown in Figure 2, the nano-multilayered film with the ZrO$_2$ layer thickness of 0.6 nm shifted to a smaller angle, suggesting that the (AlCrTiZrMo)N layers are subject to tensile stress. Therefore, the alternating stress field forms along the growth direction in the nano-multilayered films. Kato [44] stated that hardening in an fcc structure mainly occurs in the positive region of the internal stress. The corresponding increase in the film, relative to the hardness of ZrO$_2$ (ΔH_2), can be expressed as [47]

$$\Delta H = 3\sigma = \frac{\sqrt{6}}{2}\,A\varepsilon E \qquad (4)$$

where ε is the lattice mismatch between the two layers of the material. Due to the transformation of the structure of ZrO$_2$, it is difficult to calculate the lattice mismatch between (AlCrTiZrMo)N and ZrO$_2$, which takes 3~4% in this study [47]. A is the modulation amplitude of the nano-multilayered films, which is related to the modulation period and the interfacial mixing degree of the film; A takes 0.5 [48]. E is the average of the elastic moduli of the two layers of the materials and is calculated as 210.1 GPa.

According to calculation (4), the hardness increment (ΔH_2) is 3.9~5.1 GPa. Based on the theories of the elastic modulus difference and the alternating stress field, the total hardness increase ($\Delta H_1 + \Delta H_2$) in the (AlCrTiZrMo)N/ZrO$_2$ nano-multilayered film is 25.4~33.8 GPa; that is, the theoretical hardness of the film is 36.9~45.3 GPa. However, the actual maximum hardness of the (AlCrTiZrMo)N/ZrO$_2$ nano-multilayered film is 35.1 GPa, which is slightly lower than the theoretical value. This trend may be due to the structural transformation of the ZrO$_2$ layers under the coherent structure in the film, which results in a change in the modulus. The existing techniques cannot determine the modulus of a single-layer film within a nano-multilayered film, which leads to the deviation of the actual hardness from the theoretical value.

4.2. Thermal Stability of the (AlCrTiZrMo)N/ZrO$_2$ Nano-Multilayered Films

The mechanical properties of the (AlCrTiZrMo)N/ZrO$_2$ nano-multilayered films are stable after annealing below 900 °C. The hardness and elastic modulus of the (AlCrTiZrMo)N/ZrO$_2$ film with the ZrO$_2$ layer thickness of 0.6 nm after annealing at 900 °C for 30 min are nearly equivalent to those of the (AlCrTiZrMo)N film at room temperature. The optimized thermal stability of the (AlCrTiZrMo)N/ZrO$_2$ nano-multilayered film is mainly related to the following factors: the favorable thermal stability of ZrO$_2$, the lattice distortion of (AlCrTiZrMo)N, and the nano-multilayered film structure.

Firstly, ZrO_2 is a high-temperature-resistant material with low thermal conductivity. ZrO_2 layers in a nano-multilayered film can effectively prevent the diffusion of oxygen atoms, reduce the oxidation degree of the film, and improve the thermal stability of the nano-multilayered film. Secondly, high-entropy alloys have a hysteresis diffusion effect, and the diffusion is slower than that of conventional alloys [31], so the (AlCrTiZrMo)N layer can hinder the diffusion movement of oxygen atoms. Finally, there is an obvious lattice distortion at the epitaxial interface between the (AlCrTiZrMo)N and ZrO_2 layers. When oxygen atoms diffuse from one layer to another, they can be hindered by the epitaxial interface within the nano-multilayered film, reducing the diffusion rate of the oxygen atoms. Therefore, the structure of the multilayered film can effectively improve the thermal stability of the film. Furthermore, the alternating stress field along the film growth direction can also hinder the oxygen atom diffusion from the tensile stress layer to the compressive stress layer.

Hence, in future designs of nano-multilayered films, a modulation layer with good thermal stability can be selected, and HEA nitride film can be included to improve the thermal stability of the nano-multilayered film. Moreover, the thermal stability of the nano-multilayered film can be enhanced by optimizing a suitable modulation period and the formation of the epitaxial interface. Nano-multilayered films composed of HEA nitride and oxide layers are potential coating materials with good high-temperature resistance.

5. Conclusions

(1)　The (AlCrTiZrMo)N/ZrO_2 nano-multilayered film presents an fcc structure. When the ZrO_2 layer thickness increases, the peak intensity first increases and then decreases. When the thickness of the ZrO_2 layer is less than 0.6 nm, the ZrO_2 layers convert into a cubic structure and form a coherent interface with the (AlCrTiZrMo)N layer. When the thickness of the ZrO_2 layer exceeds 0.6 nm, the fcc-structured ZrO_2 layers transform back into a monoclinic structure, leading to the deterioration of the crystallization integrity.

(2)　When the film thickness of ZrO_2 increases, the mechanical properties of the nano-multilayered film first increase and then decrease. When the ZrO_2 film thickness is 0.6 nm, the maximum values of the hardness and elastic modulus are obtained, which are 35.1 GPa and 376.4 GPa, respectively. The strengthening effect can be attributed to the modulus difference between ZrO_2 and (AlCrTiZrMo)N and the alternating stress field theory. The actual hardness is slightly lower than the theoretical hardness, which may be due to the structural transformation of the ZrO_2 layers under the coherent structure in the film, resulting in a change in the modulus.

(3)　The (AlCrTiZrMo)N/ZrO_2 nano-multilayered film presents high thermal stability. The mechanical properties of the (AlCrTiZrMo)N/ZrO_2 film with the ZrO_2 layer thickness of 0.6 nm after annealing at 900 °C for 30 min are nearly equivalent to those of the (AlCrTiZrMo)N film at room temperature. The high thermal stability can be attributed to the favorable thermal stability of the ZrO_2 layer, the lattice distortion of (AlCrTiZrMo)N, and the nano-multilayered film structure.

Author Contributions: Experiment, analysis, and writing, Q.Z.; analysis, editing, supervision, and funding acquisition, W.L.; analysis and editing, P.L.; analysis and editing, W.C.; analysis and editing, K.Z.; analysis, reviewing, and editing, F.M.; analysis and editing X.C.; analysis, reviewing, and editing, R.F.; analysis, reviewing, and editing, P.K.L. All authors have read and agreed to the published version of the manuscript.

Data Availability Statement: Not applicable.

Conflicts of Interest: The authors declare no conflict of interest.

References

1. Yeh, J.W.; Chen, S.K.; Lin, S.J.; Gan, J.Y.; Chin, T.S.; Shun, T.T.; Tsau, C.H.; Chang, S.Y. Nanostructured high-entropy alloys with multiple principal elements: Novel alloy design concepts and outcomes. *Adv. Eng. Mater.* **2004**, *6*, 299–303. [CrossRef]
2. Cantor, B.; Chang, I.T.H.; Knight, P.; Vincent, A.J.B. Microstructural development in equiatomic multicomponent alloys. *Mater. Sci. Eng. A* **2004**, *375–377*, 213–218. [CrossRef]
3. Zhou, J.Y.; Zhang, Y.; Wang, F.J.; Chen, G.L. Phase transformation induced by lattice distortion in multiprincipal component CoCrFeNCuxAl1-x solid-solution alloys. *Appl. Phys. Lett.* **2008**, *92*, 241–917. [CrossRef]
4. Zhang, Y.; Zuo, T.T.; Tang, Z.; Gao, M.C.; Dahmen, K.A.; Liaw, P.K.; Lu, Z.P. Microstructures and properties of high-entropy alloys. *Prog. Mater. Sci.* **2014**, *61*, 1–93. [CrossRef]
5. Youssef, K.M.; Zaddach, A.J.; Niu, C.N.; Irving, D.L.; Koch, C.C. A Novel Low-Density, High-Hardness, High-entropy Alloy with Close-packed Single-phase Nanocrystalline Structures. *Mater. Res. Lett.* **2014**, *3*, 95–99. [CrossRef]
6. Gao, M.C.; Yeh, J.W.; Liaw, P.K.; Zhang, Y. *High-Entropy Alloys: Fundamentals and Applications*; Springer: Berlin, Germany, 2016.
7. Zhao, J.Y.; Qiao, J.W.; Ma, S.G.; Gao, M.C.; Yang, H.J.; Chen, M.W.; Zhang, Y. A hexagonal close-packed high-entropy alloy: The effect of entropy. *Mater. Des.* **2016**, *96*, 10–15. [CrossRef]
8. Senkov, O.N.; Senkova, S.V.; Woodward, C. Effect of aluminum on the microstructure and properties of two refractory high-entropy alloys. *Acta Mater.* **2014**, *68*, 214–228. [CrossRef]
9. Varalakshmi, S.; Kamaraj, M.; Murty, B.S. Processing and properties of nanocrystalline CuNiCoZnAlTi high entropy alloys by mechanical alloying. *Mater. Sci. Eng. A* **2010**, *527*, 1027–1030. [CrossRef]
10. Yu, P.F.; Zhang, L.J.; Cheng, H.; Zhang, H.; Ma, M.Z.; Li, Y.C.; Li, G.; Liaw, P.K.; Liu, R.P. The high-entropy alloys with high hardness and soft magnetic property prepared by mechanical alloying and high-pressure sintering. *Intermetallics* **2016**, *70*, 82–87. [CrossRef]
11. Liu, Y.C.; Cho, Y.H. Elucidating the microstructural and tribological characteristics of NiCrAlCoCu and NiCrAlCoMo multicomponent alloy clad layers synthesized in situ. *Surf. Coat. Technol.* **2009**, *203*, 1694–1701.
12. Chuang, M.H.; Tsai, M.H.; Wang, W.R.; Lin, S.J.; Yeh, J.W. Microstructure and wear behavior of AlxCo1.5CrFeNi1.5Tiy high-entropy alloys. *Acta Mater.* **2011**, *59*, 6308–6317. [CrossRef]
13. Chen, M.; Shi, X.H.; Yang, H.J.; Liaw, P.K.; Gao, M.C.; Hawk, J.A.; Qiao, J.W. Wear behavior of Al0.6CoCrFeNi high-entropy alloys: Effect of environments. *J. Mater. Res.* **2018**, *33*, 3310–3320. [CrossRef]
14. Hemphill, M.A.; Yuan, T.; Wang, G.Y.; Yeh, J.W.; Tsai, C.W.; Chuang, A.; Liaw, P.K. Fatigue behavior of Al0.5CoCrCuFeNi high entropy alloys. *Acta Mater.* **2012**, *60*, 5723–5734. [CrossRef]
15. Tang, Z.; Yuan, T.; Tsai, C.W.; Yeh, J.W.; Lundin, C.D.; Liaw, P.K. Fatigue behavior of a wrought Al0.5CoCrCuFeNi two-phase high-entropy alloy. *Acta Mater.* **2015**, *99*, 247–258. [CrossRef]
16. Shukla, S.; Wang, T.H.; Cotton, S.; Mishra, R.S. Hierarchical microstructure for improved fatigue properties in a eutectic high entropy alloy. *Scr. Mater.* **2018**, *156*, 105–109. [CrossRef]
17. Thurston, K.V.S.; Gludovatz, B.; Yu, Q.; Laplanche, G.; George, E.P.; Ritchie, R.O. Temperature and load-ratio dependent fatigue-crack growth in the CrMnFeCoNi high-entropy alloy. *J. Alloys Compd.* **2019**, *794*, 525–533. [CrossRef]
18. Lee, C.P.; Chang, C.C.; Chen, Y.Y.; Yeh, J.W.; Shih, H.C. Effect of the aluminium content of AlxCrFe1.5MnNi0.5 high-entropy alloys on the corrosion behaviour in aqueous environments. *Corros. Sci.* **2008**, *50*, 2053–2060. [CrossRef]
19. Shi, Y.Z.; Collins, L.; Balke, N.; Liaw, P.K.; Yang, B. In-situ electrochemical-AFM study of localized corrosion of AlxCoCrFeNi high-entropy alloys in chloride solution. *Appl. Surf. Sci.* **2018**, *439*, 533–544. [CrossRef]
20. Shi, Y.Z.; Collins, L.; Feng, R.; Zhang, C.; Balke, N.; Liaw, P.K.; Yang, B. Homogenization of AlxCoCrFeNi high-entropy alloys with improved corrosion resistance. *Corros. Sci.* **2018**, *133*, 120–131. [CrossRef]
21. Shi, Y.Z.; Yang, B.; Xie, X.; Brechtl, J.; Dahmen, K.A.; Liaw, P.K. Corrosion of Al$_x$CoCrFeNi high-entropy alloys: Al-content and potential scan-rate dependent pitting behavior. *Corros. Sci.* **2017**, *119*, 33–45. [CrossRef]
22. Li, Z.M.; Körmann, F.; Grabowski, B.; Neugebauer, J.; Raabe, D. Ab initio assisted design of quinary dual-phase high-entropy alloys with transformation-induced plasticity. *Acta Mater.* **2017**, *136*, 262–270. [CrossRef]
23. Shi, P.J.; Ren, W.L.; Zheng, T.X.; Ren, Z.M.; Hou, X.L.; Peng, J.C.; Hu, P.F.; Gao, Y.F.; Zhong, Y.B.; Liaw, P.K. Enhanced strength-ductility synergy in ultrafine-grained eutectic high-entropy alloys by inheriting microstructural lamellae. *Nat. Commun.* **2019**, *10*, 489. [CrossRef]
24. Li, W.D.; Liaw, P.K.; Gao, Y.F. Fracture resistance of high entropy alloys: A review. *Intermetallics* **2018**, *99*, 69–83. [CrossRef]
25. Gludovatz, B.; Hohenwarter, A.; Catoor, D.; Chang, E.H.; George, E.P.; Ritchie, R.O. A fracture-resistant high-entropy alloy for cryogenic applications. *Science* **2014**, *345*, 1153–1158. [CrossRef]
26. Savan, A.; Allermann1, T.; Wang, X.; Grochlal, D.; Banko, L.; Kalchev, Y.; Kostka, A. Structure zone investigation of multiple principle element alloy thin films as optimization for nanoindentation measurements. *Materials* **2020**, *13*, 2113. [CrossRef]
27. Huo, W.Y.; Liu, X.D.; Tan, S.Y.; Fang, F.; Xie, Z.H.; Shang, J.K.; Jiang, J.Q. Ultrahigh hardness and high electrical resistivity in nano-twinned, nanocrystalline high-entropy alloy films. *Appl. Surf. Sci.* **2018**, *439*, 222–225. [CrossRef]
28. Zhang, Y.; Zuo, T.T.; Cheng, Y.Q.; Liaw, P.K. High-entropy alloys with high saturation magnetization, electrical resistivity, and malleability. *Sci. Rep.* **2013**, *3*, 1455. [CrossRef] [PubMed]
29. Miracle, D.B.; Senkov, O.N. A critical review of high entropy alloys and related concepts. *Acta Mater.* **2017**, *122*, 448–511. [CrossRef]

30. Li, W.; Liu, P.; Liaw, P.K. Microstructures and properties of high-entropy alloy films and coatings: A review. *Mater. Res. Lett.* **2018**, *6*, 199–229. [CrossRef]

31. Schwarz, H.; Rösch, N.; Lindner, T.; Lampke, T.; Ganss, F.; Hellwig, O.; Lampke, T.; Wagner, G.; Seyller, T. CoCrFeNi high-entropy alloy thin films synthesized by magnetron sputter deposition from spark plasma sintered targets. *Coatings* **2021**, *11*, 468. [CrossRef]

32. Chen, T.K.; Shun, T.T.; Yeh, J.W.; Wong, M.S. Nanostructured nitride films of multi-element high-entropy alloys by reactive DC sputtering. *Surf. Coat. Technol.* **2004**, *188–189*, 193–200. [CrossRef]

33. Huang, P.K.; Yeh, J.W. Effects of nitrogen content on structure and mechanical properties of multi-element (AlCrNbSiTiV)N coating. *Surf. Coat. Technol.* **2009**, *203*, 1891–1896. [CrossRef]

34. Liang, S.C.; Tsai, D.C.; Chang, Z.C.; Sung, H.S.; Lin, Y.C.; Yeh, Y.J.; Deng, M.J.; Shieu, F.S. Structural and mechanical properties of multi-element (TiVCrZrHf)N coatings by reactive magnetron sputtering. *Appl. Surf. Sci.* **2011**, *258*, 399–403. [CrossRef]

35. Koehler, J.S. Attempt to Design a Strong Solid. *Phys. Rev. B* **1970**, *2*, 547–551. [CrossRef]

36. Yang, W.M.C.; Tsakalakos, T.; Hilliard, J.E. Enhanced elastic modulus in composition-modulated gold-nickel and copperpalladium foils. *J. Appl. Phys.* **1977**, *48*, 876–879. [CrossRef]

37. Chu, X.; Wong, M.S.; Sproul, W.D.; Barnett, S.A. Mechanical properties and microstructures of polycrystalline ceramic/metal superlattices: TiN/Ni and TiN/Ni0.9Cr0.1. *Surf. Technol.* **1993**, *61*, 251–256. [CrossRef]

38. Liu, M.; Yang, Y.; Mao, Q.; Wei, Y.q.; Li, Y.J.; Ma, N.N.; Liu, H.; Liu, X.J. Influence of radio frequency magnetron sputtering parameters on the structure and performance of SiC films. *Ceram. Int.* **2021**, *47*, 24098–24105. [CrossRef]

39. Li, W.; Liu, P.; Zhao, Y.S.; Ma, F.C.; Liu, X.K.; Chen, X.H.; He, D.H. Structure, mechanical properties and thermal stability of CrAlN/ZrO$_2$ nanomultilayers deposited by magnetron sputtering. *J. Alloys Compd.* **2013**, *562*, 5–10. [CrossRef]

40. Chen, H.; Zhou, X.M.; Ding, C.X. Investigation of the thermomechanical properties of a plasma-sprayed nanostructured zirconia coating. *J. Eur. Ceram. Soc.* **2003**, *23*, 1449–1455. [CrossRef]

41. Yue, J.L.; Liu, Y.; Li, G.Y. Template-induced coherent growth and mechanical properties of ZrO$_2$/TiN nano-multilayers. *Scr. Mater.* **2009**, *60*, 240–243. [CrossRef]

42. Kim, I.W.; Li, Q.; Marks, L.D.; Barnett, S.A. Critical thickness for transformation of epitaxially stabilized cubic AlN in superlattices. *Appl. Phys. Lett.* **2001**, *78*, 892–894. [CrossRef]

43. Chu, X.; Bamett, S.A.; Wong, M.S.; Sproul, W.D. Reactive unbalanced magnetron sputter deposition of polycrystalline TiN/NbN superlattice coatings. *Surf. Coat. Technol.* **1993**, *57*, 13–18. [CrossRef]

44. Kato, M.; Mori, T.; Schwartz, L.H. Hardening by spinodal modulated structure. *Acta Met.* **1980**, *28*, 285–290. [CrossRef]

45. Pacheco, E.S.; Mura, T. Interaction between a screw dislocation and a bimetallic interface. *J. Mech. Phys. Solids* **1969**, *17*, 163–170. [CrossRef]

46. Chu, X.; Barnett, S.A. Model of superlattice yield stress and hardness enhancements. *J. Appl. Phys.* **1995**, *77*, 4403–4411. [CrossRef]

47. Li, W.; Liu, P.; Xue, Z.H.; Ma, F.C.; Zhang, K.; Chen, X.H.; Feng, R.; Liaw, P.K. Microstructures, mechanical behavior and strengthening mechanism of TiSiCN nanocomposite films. *Sci. Rep.* **2017**, *7*, 2140. [CrossRef]

48. Shinn, M.; Barnett, S.A. Effect of superlattice layer elastic moduli on hardness. *Appl. Phys. Lett.* **1994**, *64*, 61–63. [CrossRef]